ingegneria sismica
International Journal of Earthquake Engineering
Anno XLIII - Num. 1 - 2026

Synchronization signal analysis of multi-channel grating sensor system based on digital signal processing algorithm

Yu Ge[1,*]

[1] Yuzhang Normal College, Nanchang, Jiangxi, 330103 China

SUMMARY: *In order to support synchronous analysis in multi-channel fiber Bragg grating sensing systems, a digital signal processing framework is constructed, which integrates synchronous acquisition, delay estimation, fractional compensation, adaptive* denoising, *window alignment and spectral peak tracking. The system organizes 16 sensing channels and 48,000 segments of synchronization signals under the strain-temperature coupling condition, and constructs a unified process of sampling control, time registration, feature extraction and cross-channel consistency evaluation. The reference channel selection, phase correlation delay estimation and fractional resampling constitute the link. Combined with threshold denoising and consensus update, the wavelength demodulation is stabilized and the time shift drift under high-frequency sampling is suppressed. Experimental results show that the synchronization error of the proposed method is 0.37 ms, the wavelength demodulation accuracy is 98.9%, the F1-score of peak identification is 97.6%, and the cross-channel variance suppression rate is 21.4%. The hardware and software system maintains the processing speed of 2.8×105 sample points per second, and provides support for the calculation of synchronization signals of multi-channel perception scenes.*

KEYWORDS: *Multi-channel grating sensor system; Digital signal processing; Synchronization signal analysis; Wavelength demodulation*

1 Introduction

Multi-channel grating sensor system undertakes continuous acquisition and precision measurement tasks in structure monitoring, equipment diagnosis and industrial process perception. With the increase of the number of sensor nodes and the increase of the sampling frequency, the reflection spectra, power sequences and wavelength shifts from different channels at the same time need to be received, registered, demodulated and calculated under a unified time reference, which makes the analysis of synchronization signals gradually become the core part of the system performance evaluation. Digital signal processing algorithms have the advantages of time sequence alignment, noise suppression, spectral peak tracking and multi-channel consistency modeling, which can transform the continuous response in optical sensing links into computable, comparable and reproducible data representation, and provide stable support for real-time analysis of multi-channel grating sensing systems.

Around the grating sensing demodulation and computational modeling, related research has formed a relatively clear technical path. Chen et al. studied the wavelength demodulation process of fiber Bragg grating based on array waveguide grating, and used the cascade neural network to improve the interrogation performance, which enhanced the demodulation

*geyu830814@163.com
https://doi.org/10.65102/is2026350
Published: 30 April, 2026

accuracy and stability of the system under the condition of low cost [1]. Cao et al. proposed a grating sensing spectrum demodulation method based on deep convolutional neural network, which combined spectral mapping and feature learning to improve the wavelength identification ability under complex spectral shape conditions [2]. Li et al. studied the design of PLC-type array waveguide grating for fiber Bragg grating interrogation system, which provided device level support for multi-channel parallel demodulation [3]. Poiana et al. proposed a compact grating sensing interrogation system based on multiple heterodyne dispersive interference, and realized high-speed signal reading in dynamic strain measurement scene [4]. Huang et al. studied a high-precision grating temperature demodulation system based on optical power detection, so that the signal analysis after photoelectric conversion has a higher resolution [5]. Dey et al. proposed a machine learning method for simultaneous measurement of strain and temperature, which expanded the computational expression of grating sensing data in multi-parameter estimation [6]. Li et al. studied a wavelength demodulation system cascaded by generative adversarial network and dense neural network, which strengthened the feature recovery ability under weak signal conditions [7]. Weng et al. proposed a SOI array waveguide grating structure with extended dynamic range, which makes the demodulation link maintain strong adaptability in a highly dynamic sampling environment [8]. Ren et al. studied a high-efficiency grating array interrogation system based on the cooperation of sparse data and neural network, which reduced the sampling burden while maintaining the demodling accuracy [9].

The existing results provide a reliable basis for efficient sampling, wavelength demodulation and data reconstruction of multi-channel grating sensing systems, and also promote the extension of optoelectronic sensing to intelligent computing. However, from the perspective of multi-channel synchronous analysis, the system operation process involves not only single-channel spectral shape recognition, but also cross-channel time reference unification, sampling delay correction, asynchronous drift compensation, frequency domain response matching and result consistency calculation. Only by organizing the output of acquisition control, digital filtering, synchronous registration, feature extraction and analysis as a complete computing link, can a stable joint representation of multi-channel signals be formed in the same software framework.

This paper focuses on the synchronous signal analysis process of multi-channel grating sensor system, and constructs a calculation method for digital signal processing. The research content includes multi-channel synchronous acquisition and digital signal modeling, algorithm design for synchronization error suppression, and system implementation and analysis process construction. The corresponding experimental part is verified from two levels of algorithm performance and system performance, which is used to investigate the synchronization error control effect, channel consistency and real-time processing ability. At the level of computing implementation, the synchronous analysis tasks are processed in a unified data stream, and the buffer queue management, window segmentation, time series index update and parallel feature calculation mechanisms are adopted to make the sensor input, algorithm execution and result output have a clear software interface. At the implementation level, the synchronous analysis tasks are processed in a unified data stream. Through buffer queue management, window segmentation, time series index update and parallel feature calculation, the sensor input, algorithm execution and result output form a coherent calculation process.

2 Related work

In recent years, the research of multi-channel grating sensor system has gradually expanded from a single demodulation structure to parallel acquisition, on-chip integration, intelligent decoding and distributed cooperative computing. The relevant achievements provide a multi-level technical foundation for synchronization signal analysis. Li et al. studied the design of SOI 15-channel array waveguide grating for fiber Bragg grating interrogator, and enhanced the parallel wavelength separation capability by optimizing channel spacing and transmission structure [10]. Jiao et al. proposed a high-precision parallel AWG demodulation system, which combined the parallel readout mechanism with the high-resolution measurement link to improve the consistency and accuracy of multi-channel demodulation [11]. Inaba et al. studied the grating interrogation method of time division multiplexing and wavelength division multiplexing based on dual-wavelength differential detection, so that multi-channel grating signals could be multiplexed and read within a unified sampling framework [12]. Chen et al. proposed a full-on-chip integrated FBG interrogator structure, and designed the compression hardware link length through high-precision wavelength measurement, which provided the implementation basis for a compact synchronous acquisition system [13].

Focusing on the improvement of demodulation accuracy and algorithm-aided calculation, related studies have further introduced machine learning methods into grating sensor data processing. Yue et al. studied the interrogation method of array waveguide grating fiber Bragg grating assisted by random forest, and used nonlinear mapping to improve the demodulation performance [14]. Yue et al. also proposed a large-dynamic range optical fiber interference sensing interrogation technology based on AWG and deep learning algorithm to maintain a high degree of stability in the demodulation process in the complex response interval [15]. This kind of research shows that there is a close cooperative relationship between the optical readout structure and the data-driven model, and the performance evaluation of the sensing system is extended from a single hardware index to a multi-dimensional index such as demodulation error, response range and computational robustness.

As shown in Table 1, the existing methods have covered multiple directions such as multi-channel device design, parallel demodulation structure, integrated readout and learning-assisted decoding, and different studies have formed a clear differentiation in system configuration and calculation path.

Table 1: Summary of related work

Researcher	Main Contribution	Computational Focus	Result Characteristics
Li et al.	Design of a fifteen-channel SOI arrayed waveguide grating	Parallel wavelength separation	Stable channel structure
Jiao et al.	High-precision parallel AWG demodulation system	Parallel measurement link	High demodulation accuracy
Inaba et al.	Time-division and wavelength-division multiplexing interrogation method	Unified sampling organization	Effective multiplexed reading
Chen et al.	On-chip integrated FBG interrogator	Compact computational interface	High measurement accuracy
Yue et al.	Random-forest-assisted demodulation	Nonlinear mapping learning	Enhanced performance
Yue et al.	Deep-learning-based large dynamic range interrogation	Complex response modeling	Extended dynamic range
Hou et al.	Federated-learning-based wavelength demodulation	Distributed parameter collaboration	Suitable for multi-point scenarios

In terms of multi-point distribution, overlapping spectrum processing, and system extension, recent research continues to advance in the direction of computational collaboration. Hou et al. studied the multi-point distributed multi-peak FBG wavelength demodulation system based on federated learning, and enhanced the model sharing ability between different nodes through the distributed parameter update mechanism [16]. Li et al. proposed a double-sided input MMI AWG high-performance interrogator to make a better match between input structure and signal output efficiency [17]. Ding et al. studied the FBG interrogator based on dispersive waveguide chip and CMOS camera, which combined image sensing and spectrum reading, and expanded the data representation method of signal acquisition [18]. Liu et al. proposed a two-stage deep learning demodulation method for highly overlapping grating sensor networks to maintain the stability of the demodulation process under complex spectral peak overlap conditions [19]. Xu et al. studied a multi-channel AWG-type FBG interrogation system using a one-by-four MEMS optical switch, so that channel switching and multi-channel reading were organized in a unified system [20].

Synthesizing the existing results, it can be seen that the related research has formed a continuous technology chain from device structure, parallel demodulation to intelligent computing. The existing works pay full attention to the accuracy of wavelength readout, the extension of dynamic range and the efficiency of multi-point demodulation, and also lay the foundation for the data acquisition of multi-channel grating sensor system. In contrast, researches directly oriented to synchronization signal analysis pay more attention to channel registration, sampling delay compensation, cross-channel feature consistency calculation and real-time software link organization under a unified time reference. The related work of this paper is based on this background, and the subsequent research emlays digital signal processing algorithm into the whole process of multi-channel acquisition, synchronous correction and result analysis, so as to form a more complete calculation implementation path.

3 Synchronous signal analysis method of multi-channel grating sensor system based on digital signal processing algorithm

3.1 Synchronous acquisition and digital signal modeling of multi-channel raster

Multi-channel raster synchronous acquisition does not simply stack multiple sensing channels to the same read port, but organizes the spectral response, trigger timing, cache writing and feature generation into a continuous data processing chain. In order to ensure that the subsequent digital signal processing algorithm can directly call the original input of each channel, the system sets a unified master clock, channel multiplexer, high-speed analog-to-digital conversion unit and buffer control module at the acquisition end, and writes the reflection spectrum, amplitude sequence and time label in each sampling period into the shared memory area. After this process, the original sampled values are no longer scattered records, but structured samples with channel numbers, timestamps, and state markers.

In order to clearly illustrate the transfer relationship among the acquisition end, the conversion end and the modeling end of the multi-channel raster signal, the synchronous sampling, buffer organization and feature generation process are unified in this paper. As shown in Fig. 1, the excitation and return of multi-channel grating reflected signals are completed on the left side of the system, and the responses of different grating channels are

multiplexed and entered into the photoelectric conversion module to form analog electrical signals for sampling. In the middle part, an analog-to-digital conversion unit driven by a unified clock performs discretization acquisition, and synchronously records the timestamp, channel number and trigger position of each batch of data, so that the original input forms a traceability data block in the buffer area. The computing layer on the right side completes the spectral peak location, state update and feature encapsulation in turn, and organizes the discrete sampling values into tensor objects suitable for algorithm calls.

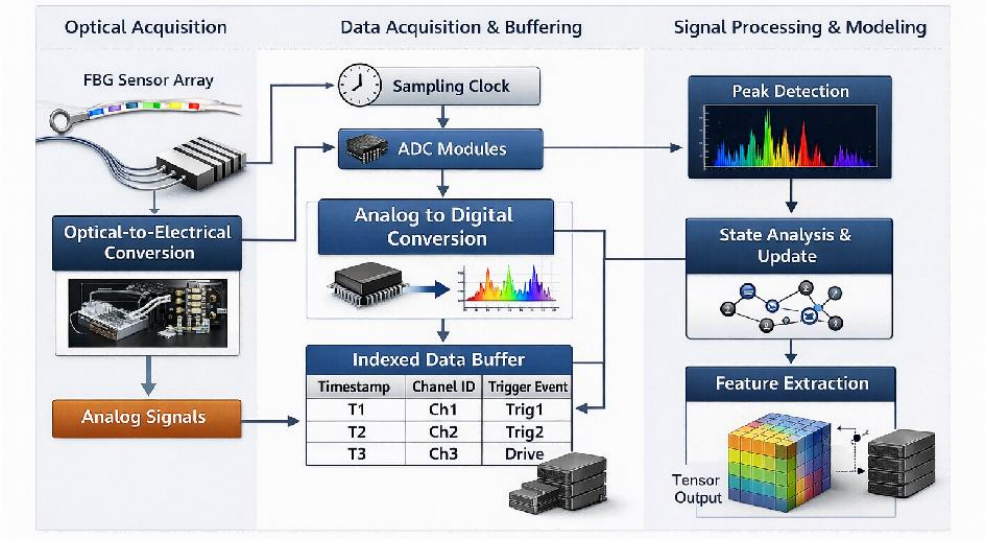

Figure 1: Multi-channel raster synchronous acquisition and digital signal modeling process

Driven by a unified clock, the simulated response of each channel can be written as a discrete sequence after sampling. The channel gain, sampling delay and random disturbance together form the basic form of the original input:

$$x_c[n] = \alpha_c\, r_c(nT_s + \delta_c) + \beta_c + \varepsilon_c[n], \quad c = 1,2,\dots,C \tag{1}$$

Here, $x_c[n]$ represents the sampled value of the c channel at the n discrete time, α_c represents the channel gain coefficient, r_c represents the original reflection response, T_s represents the sampling period, δ_c represents the sampling delay, β_c represents the DC bias, and $\varepsilon_c[n]$ represents the random disturbance. This formula formulates the parallel sampling process as a unified discrete model, which provides the basis for subsequent calibration and registration.

In order to reduce the scale differences caused by different channel magnification and baseline drift, the sampling sequence needs to be normalized and compressed before entering the unified analysis window, which is expressed as follows.

$$\tilde{x}_c[n] = \frac{x_c[n] - \mu_c}{\sqrt{\sigma_c^2 + \lambda \sum_{k=1}^{K} (x_c[n-k] - x_c[n])^2}} \tag{2}$$

Here, $\tilde{x}_c[n]$ represents the normalized sequence, μ_c represents the channel mean, σ_c^2 represents the channel variance, λ represents the local smoothing weight, and K represents the neighborhood length. This formula preserves the relative fluctuation of the spectral peak and compresses the amplitude drift at the same time, making the multi-channel data more suitable for entering the unified analysis window.

After amplitude normalization, the center position of the spectral peak needs to be further estimated from the local search interval. The center wavelength of the reflected peak can be expressed by the weighted centroid method as follows.

$$\hat{\lambda}_c[t] = \frac{\sum_{m\in\Omega_c} \lambda_m \; p_c(\lambda_m, t)^{\gamma}}{\sum_{m\in\Omega_c} p_c\,(\lambda_m, t)^{\gamma}} \tag{3}$$

Here, $\hat{\lambda}_c[t]$ represents the estimated central wavelength of the c channel at time t, Ω_c represents the spectral peak search interval, λ_m represents the discrete wavelength point, p_c represents the optical power of the corresponding wavelength, and γ represents the enhancement index. By increasing the contribution of samples near the main peak, this formula reduces the interference of edge noise on the center location.

Considering the continuity of wavelength change between adjacent moments, the current sampling result needs to be updated with the previous state. The recursive process of channel state can be written as follows.

$$z_c[t] = \eta z_c[t-1] + (1-\eta)\hat{\lambda}_c[t] + \rho(\hat{\lambda}_c[t] - \hat{\lambda}_c[t-1]) \tag{4}$$

Here, $z_c[t]$ represents the channel state variable, η represents the history retention coefficient, ρ represents the slope compensation coefficient, and $\hat{\lambda}_c[t]$ and $\hat{\lambda}_c[t-1]$ represent the wavelength estimates at the current and previous time instants, respectively. This formula combines the instantaneous measurement with the historical trend, and can suppress the short-time jump caused by the sampling jitter.

In order to further describe the time-frequency distribution characteristics of the multi-channel response in the local window, the detrend sequence can be mapped to the joint time-frequency space, and its energy can be expressed as follows.

$$E_c(u,\omega) = \left| \sum_{n=0}^{N-1} \bar{x}_c[n]\, w[n-u] e^{-j\omega n} \right|^2 \tag{5}$$

Here, $E_c(u,\omega)$ represents the local energy of the c channel at time position u and angular frequency ω, $\bar{x}_c[n]$ represents the detrend sequence, and w represents the analysis window function. This equation maps the time-domain response to the local spectrum space, which is beneficial to identify the difference between the fast disturbance and the synchronous offset in the frequency domain.

In the synchronization analysis stage, time deviation, central wavelength difference and time-frequency feature similarity need to be uniformly encoded into the same discriminant, so the cross-channel consistency score can be expressed as follows.

$$q_{ij}[t] = \omega_1 e^{-|\Delta\tau_{ij}[t]|/\kappa_1} + \omega_2 e^{-|\Delta\lambda_{ij}[t]|/\kappa_2} + \omega_3 \frac{\langle e_i[t], e_j[t]\rangle}{\|e_i[t]\|_2 \, \|e_j[t]\|_2} \tag{6}$$

Here, $q_{ij}[t]$ represents the synchronization consistency score between channel i and channel j at time t, $\Delta\tau_{ij}[t]$ represents the time deviation, $\Delta\lambda_{ij}[t]$ represents the center wavelength difference, $\langle e_i[t], e_j[t]\rangle$ represents the time-frequency feature inner product, and ω_1, ω_2, ω_3 represent the weight coefficients. The formula writes the time, wavelength and feature similarity into the same discriminant, which is convenient for the synchronous

analysis module to call directly.

Through the above modeling process, the raw reflection response of the multichannel raster sensing system is gradually converted into a collection of digital objects with a unified time reference, a unified amplitude scale, and a unified feature structure. This process not only retains the independent spectral peak evolution information of each channel, but also establishes a directly comparable synchronization relationship between different channels, which provides a stable input for subsequent synchronization error suppression, feature registration and system-level analysis.

3.2 Digital signal processing algorithms for Synchronization error suppression

Multi-channel grating sensor system is affected by clock jitter, channel delay, spectral peak distortion and local high frequency noise in parallel sampling. Synchronization error suppression is not a single path compensation, but a continuous process of delay estimation, score correction, noise suppression, sequence alignment and multi-channel joint correction. To this end, a digital signal processing link is constructed, which consists of reference channel selection, delay calculation, fractional time-shift compensation, time-frequency correction and consensus output, so that different channels can complete resampling and joint analysis under a unified time reference. The algorithm flow for synchronization error suppression is shown in Fig. 2. The entry of the algorithm firstly selects the reference channel with high stability from the multi-channel buffer block, and then performs phase correlation delay estimation on the remaining channels to obtain the initial time shift parameters. The compensation module completes the score-level resampling according to the time-shift results, and then performs adaptive threshold denoising and sequence alignment update in a local window. In addition to the corrected wavelength sequence, the end output also retains the residual, similarity and alignment cost for subsequent synchronization analysis and improves the interpretability of the output results.

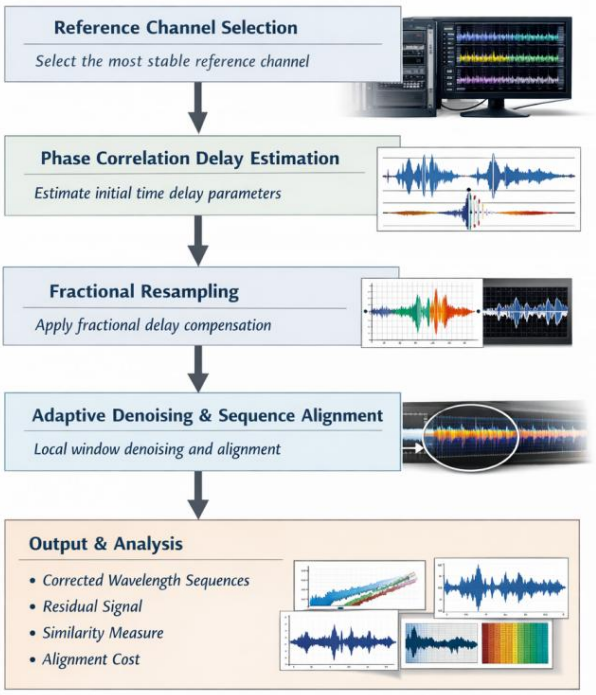

Figure 2: Digital signal processing algorithm flow for synchronization error suppression

After the multi-channel discrete modeling is completed, the synchronization error first shows that the phase response between channels is inconsistent with the peak arrival position, so the delay estimation is established first:

$$\hat{\tau}_{ij}[t] = \arg\max_{\tau\in\Gamma} \mathcal{F}^{-1}\left(\frac{X_i(\omega,t)X_j^*(\omega,t)}{|X_i(\omega,t)X_j^*(\omega,t)| + \epsilon}\right) \tag{7}$$

Here, $\hat{\tau}_{ij}[t]$ represents the delay estimation of channel i relative to channel j at time t, X_i and X_j represent the frequency domain response, $\mathcal{F}^{-1}$ represents the inverse transform operator, Γ represents the search interval, and ϵ represents the stability term. This formula uses phase correlation to suppress amplitude differences and makes the initial time shift estimation dependent on structural information.

After obtaining the initial time shift, there is still a non-integer delay between the sampling points, and the compensation module needs to perform fractional time shift reconstruction in the discrete domain to restore the channel alignment state:

$$y_i[n] = \sum_{m=-M}^{M} x_i[n-m]\,\mathrm{sinc}(m-\hat{\tau}_i)\exp\left(-\frac{(m-\hat{\tau}_i)^2}{2\sigma_h^2}\right) \tag{8}$$

Here, $y_i[n]$ represents the compensated sequence, $x_i[n]$ represents the original input, $\hat{\tau}_i$ represents the time shift to be compensated, M represents the interpolation radius, and σ_h represents the kernel width. This formula combines the ideal fractional delay with Gaussian weighting, and can complete the reconstruction in a finite window.

After the time shift compensation is completed, the local noise will still change the shape of the spectral peak edge, so it is necessary to introduce an adaptive shrinkage function to stabilize the overall output value of subsequent feature extraction:

$$u_i[n] = \mathrm{sgn}(y_i[n])\max(|y_i[n]| - \lambda_i[n], 0), \quad \lambda_i[n] = \kappa\frac{\sigma_i[n]\sqrt{2\ln N}}{1+\rho_i[n]} \tag{9}$$

Here, $u_i[n]$ represents the contracted sequence, $\lambda_i[n]$ represents the local threshold, κ represents the regulation coefficient, $\sigma_i[n]$ represents the noise intensity estimate, and $\rho_i[n]$ represents the local SNR index. This formula dynamically adjusts the threshold according to the window state, so that the strong response is retained and the weak disturbance is compressed.

After the alignment sequence enters the window analysis phase, the local rhythms of different channels need to continue to match, so the cumulative cost update step must be synchronized in the calculation:

$$D_{ij}(p,q) = \delta_{ij}(p,q) + \min\{D_{ij}(p-1,q), D_{ij}(p,q-1), D_{ij}(p-1,q-1)\} \tag{10}$$

Here, $D_{ij}(p,q)$ represents the cumulative alignment cost between channel i and channel j at grid position (p,q), and $\delta_{ij}(p,q)$ represents the local sample distance. This formula recursively accumulates the matching cost along the temporal grid so that the local rhythm differences are constrained at the window level.

After window-level registration, the multi-channel results need to be jointly corrected at the overall level, so the final output expresses the results uniformly in the form of graph constrained optimization:

$$\min_{z} \sum_{i=1}^{C} \| z_i - s_i \|_2^2 + \alpha \sum_{(i,j)\in\mathcal{E}} w_{ij} \| z_i - z_j \|_2^2 + \beta \sum_{i=1}^{C} \| \nabla_t z_i \|_1 \tag{11}$$

Here, z represents the synchronization output after joint correction, s_i represents the window-level correction result, $\mathcal{E}$ represents the set of channel connections, w_{ij} represents the edge weights, ∇_t represents the time gradient operator, and α and β represent the weight coefficients. This formula simultaneously configures data fidelity, cross-channel smoothness, and temporal continuity, making the results more suitable for entering the system-level analysis module.

After the above processing, the synchronization error of multi-channel signal is decomposed into five levels: delay estimation, fractional compensation, threshold shrinkage, local registration and global correction. The output of the algorithm retains the wavelength variation trend, correction residual and matching cost, which provides the intermediate states that can be directly called for subsequent system implementation and process analysis. On this basis, the next section will continue to expand the multi-channel grating sensing system implementation and synchronization signal analysis process.

3.3 Multi-channel grating sensing system implementation and synchronization signal analysis process

The implementation of multi-channel raster sensor system is not to concatenate the acquisition, compensation and output modules in turn, but to organize the drive control, buffer scheduling, synchronization correction, feature encapsulation and result discrimination into a unified software execution link. In order to ensure that the synchronization signal analysis can run stably under the condition of continuous input, the system uses a hierarchical structure to complete the data access and calculation distribution. The middle layer is responsible for buffer management, timestamp registration and synchronization error suppression. The upper layer is responsible for wavelength sequence generation, consistency analysis and result visualization. Each module transmits data blocks through message queue and shared memory, so that the sampling end and the computing end maintain continuous cooperation.

Fig. 3 shows the overall system implementation and synchronization signal analysis process. The acquisition driver layer is responsible for generating unified clock and trigger signal, and sends the raw response of different grating channels to the analog to digital conversion interface. The channel control and cache layer completes data block registration, batch division and buffer refresh according to the timing tag to avoid write blocking under high-frequency sampling conditions. The synchronous correction and feature layer invokes the error suppression algorithm constructed above to perform score compensation, window reorganization, and feature vector encapsulation on the input sequence. The analysis output layer writes the center wavelength, residual index and consistency score of each channel into the database and pushes them to the visualization interface synchronously. This implementation converts the hardware sampling behavior into software schedulable object, which is convenient to complete the synchronization signal analysis in a unified flow. During process execution, the system also retains the original sequence index, corrected version number, and analysis log for each batch to facilitate subsequent playback, error tracking, and parameter reset. The design enables the same batch of data to not only support service discrimination, but also support off-line review and model re-tuning, which enhances the maintainability, traceability and engineering deployment stability of the system implementation process. At the same time, the state table records the last successful alignment

time of each channel and the trend of residual change, which is used for fast initialization in the next cycle. This design further enhances process continuity.

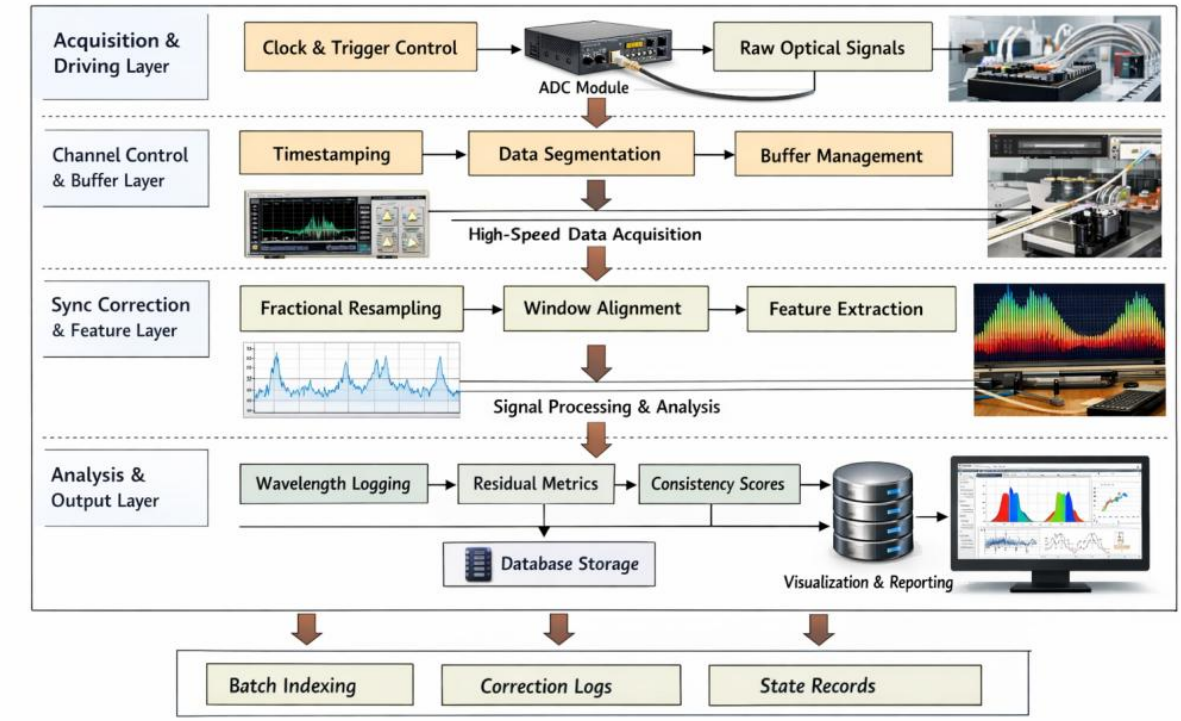

Figure 3: Multi-channel grating sensing system implementation and synchronization signal analysis process

In the process of system operation, the original data block needs to be encapsulated uniformly. The channel number, time label and window position are written into the same structure, and its data packet is expressed as:

$$B_t = \{(c_n, \tau_n, x_n, m_n) \mid n = 1,2, \dots, N_t\} \tag{12}$$

Here, B_t represents the batch of packets at time t, c_n represents the channel number, τ_n represents the time label, x_n represents the sampling sequence, m_n represents the window meta information, and N_t represents the number of samples in this batch. This formula is used to uniformly describe the data objects received by the system in a single scheduling cycle, which is convenient for subsequent distribution processing.

In order to make different types of tasks obtain reasonable computing resources in the same cycle, the cache scheduling module calculates task allocation scores according to delay, data volume and confidence priority, and its scheduling expression is as follows.

$$S_i = \frac{\phi_i \log(1 + L_i)}{1 + \exp(-\nu_i)} + \chi_i \frac{Q_i}{Q_{max}} + \psi_i \frac{A_i}{A_{max}} \tag{13}$$

Here, S_i represents the scheduling score of type i tasks,L_i represents the waiting time, ν_i represents the synchronization confidence index, Q_i represents the queue length, A_i represents the analysis priority value, and ϕ_i, χ_i, and ψ_i are weight parameters. This formula takes timeliness and reliability into the scheduling decision at the same time, so that high-frequency channels will not occupy all the computing resources for a long time.

In order to facilitate the comparison of the input-output relationship of different modules, the key processing links and corresponding functions of the system can be sorted out as shown in Table 2.

Table 2: Correspondence between key modules and functions of the system

Module Name	Input Content	Core Processing	Output Result
Acquisition Driver Layer	grating reflection response, trigger signal	clock generation, ADC sampling	raw discrete sequence
Channel Control and Buffer Layer	sampled sequence, time labels	queue scheduling, batch encapsulation	structured data blocks
Synchronization Correction and Feature Layer	data blocks, reference channel	time-shift compensation, window alignment, feature extraction	corrected sequences and feature tensors
Analysis Output Layer	correction results, similarity indicators	consistency discrimination, result database writing, interface pushing	wavelength results and analysis report

In the case of continuous sampling, the processing delay of each batch of the system is composed of four parts: acquisition, transmission, correction, and write back. Therefore, the overall response time can be written as follows.

$$T_{sys}(t) = T_{acq}(t) + T_{buf}(t) + T_{cal}(t) + T_{out}(t) + \zeta \sum_{k=1}^{K_t} \Delta_k^2 \tag{14}$$

where $T_{sys}(t)$ represents the total system delay, $T_{acq}(t)$ represents the acquisition delay, $T_{buf}(t)$ represents the cache scheduling delay, $T_{cal}(t)$ represents the synchronization correction delay, $T_{out}(t)$ represents the result writing back delay, Δ_k represents the local waiting difference within the batch, and ζ is the penalty coefficient. This formula can directly describe the influence of different processing steps on real-time performance.

Before entering the result analysis, the corrected multi-channel features also need to be fused in a unified space. The system uses gated mapping to generate the final analysis vector, and the calculation process is as follows:

$$h_t = \sum_{c=1}^{C} \frac{\exp(u^\top \tanh(W_1 f_{c,t} + W_2 g_t))}{\sum_{j=1}^{C} \exp(u^\top \tanh(W_1 f_{j,t} + W_2 g_t))} f_{c,t} \tag{15}$$

Here, h_t represents the fusion vector at time t, $f_{c,t}$ represents the local features of the c channel, g_t represents the global state vector, and W_1, W_2, and u are the mapping parameters. This formula dynamically adjusts the contribution of each channel according to the global state, so that the result analysis is more suitable for the difference of multi-channel inputs.

In order to create interpretable output grades for the synchronous analysis results, the system further maps the residual, correlation, and stability jointly into confidence scores, whose discriminant function can be written as follows.

$$P_t = \sigma(\theta_1 \bar{r}_t + \theta_2 \bar{\rho}_t + \theta_3 \bar{s}_t - \theta_4 \bar{e}_t) \tag{16}$$

Here, P_t represents the analytical confidence score at time t, $\sigma(\cdot)$ represents the Sigmoid function, $\bar{r}_t$ represents the average correlation, $\bar{\rho}_t$ represents the stability index, $\bar{s}_t$ represents the mean consistency, $\bar{e}_t$ represents the residual strength, and θ_1 to θ_4 represent the discriminant parameters. This formula makes the synchronization result not only stop at the numerical output level, but form a comparable state level.

At the software deployment level, the system throughput is also related to the number of parallel threads and the channel size, so the effective processing rate per unit time can be further expressed as follows.

$$R_{eff} = \frac{\Omega C M}{\Omega + \lambda_c C + \lambda_m M + \lambda_q \log(1 + Q)} \tag{17}$$

Here, R_{eff} represents the effective processing rate, Ω represents the basic computing power, C represents the number of channels, M represents the number of parallel threads, Q represents the average queue length, and λ_c, λ_m, and λ_q represent the complexity coefficient. This formula is used to describe the performance changes of the system under the condition of channel expansion and multi-thread deployment, and provides a calculation basis for subsequent experimental analysis.

Through the above implementation, the multi-channel raster sensor system organizes the acquisition control, buffer management, synchronization correction, feature fusion and result discrimination into a complete software calculation process. The diagram structure illustrates the logic of data transfer between layers, the table summarizes the input and output relationships of key modules, and the formula further clarifies the computational basis of data encapsulation, task scheduling, delay estimation, feature fusion, result discrimination and throughput modeling. The system implementation framework formed in this way can provide stable support for subsequent algorithm performance testing and system synchronization analysis testing.

4 Synchronous signal analysis results of multi-channel grating sensor system based on digital signal processing algorithm

4.1 Performance testing of synchronous signal processing algorithms

In order to verify the analysis effect of the proposed synchronization signal processing algorithm in the multi-channel grating sensor system, this paper carries out a comparative test based on the 16-channel synchronous acquisition data. The test data contains 48000 valid synchronization signal segments, covering various operating conditions such as strain variation, temperature disturbance and channel delay offset. The comparison methods include the basic interpolation method, the delay estimation method, the time-frequency compensation method and the proposed method. The basic interpolation method only performs uniform resampling and does not participate in synchronous correction. The delay estimation method adds hour time shift compensation on the basis of resampling. The time-frequency compensation method further introduced the local spectral domain noise suppression. The proposed method adds fractional time-shift correction, window alignment and cross-channel consistency update on the basis of the above processing. The evaluation indexes are synchronization error, wavelength demodulation accuracy, F1 value of peak identification and cross-channel variance suppression rate to reflect the actual performance of

the algorithm in time registration, spectral peak preservation and channel cooperative analysis.

In order to intuitively show the alignment effect of the proposed method in the process of multi-channel synchronization correction, the alignment distribution of representative channels after synchronization analysis is counted, and the results are shown in Fig. 4.

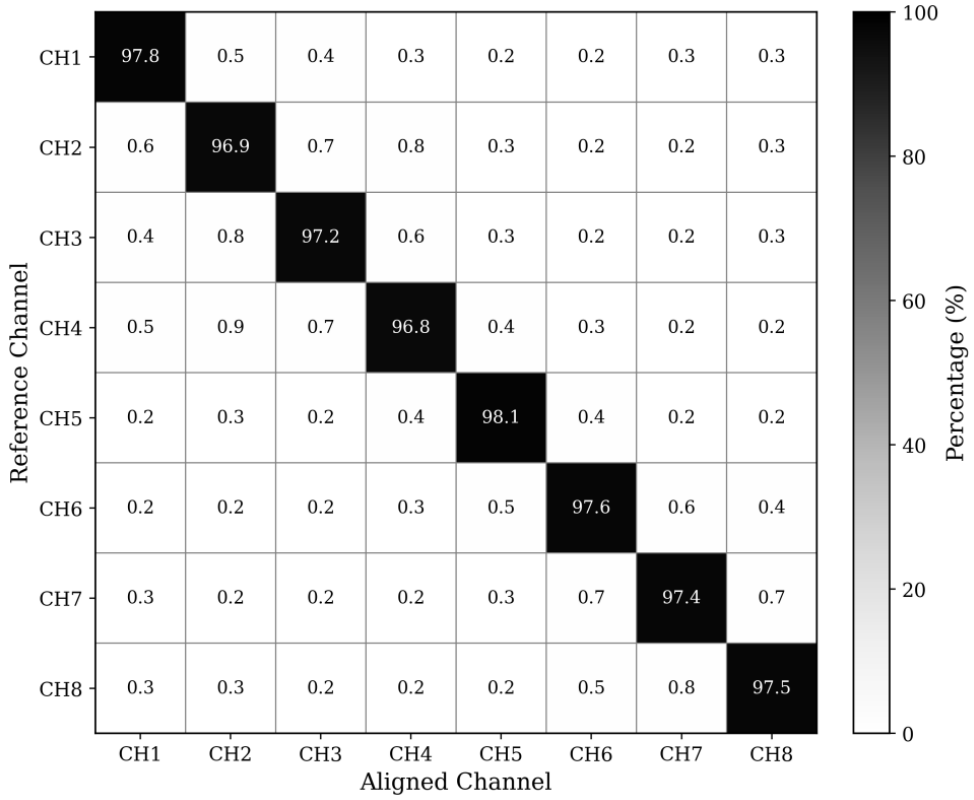

Figure 4: Matrix diagram of channel synchronization alignment results of the proposed method

The synchronous alignment results of the proposed method on the representative channels CH1-CH8 are mainly concentrated in the diagonal region of the matrix, and the diagonal elements remain at a high level, reaching 97.8%, 96.9%, 97.2%, 96.8%, 98.1%, 97.6%, 97.4% and 97.5%, respectively. In contrast, the off-diagonal region has an overall low value, mostly staying within 1.0%, with only a weak cross response between individual adjacent channels. This shows that after delay estimation, fractional time-shift compensation, local time-frequency correction and consistency update, the primary responses of each channel can accurately return to the corresponding alignment position, and the cross-channel mismatch phenomenon is significantly compressed. Fig. 4 reflects that the proposed method has strong time alignment ability and channel discrimination ability in the process of multi-channel synchronization correction, and also shows that the multi-stage error suppression link constructed in the previous section can stably support the synchronization signal analysis task.

After the synchronization error is controlled, the algorithm also needs to ensure that the wavelength demodulation and peak identification process is not weakened by the correction step. To this end, this paper continues to compare the loss changes of each method in the training phase and observe the convergence process, and the results are shown in Fig. 5.

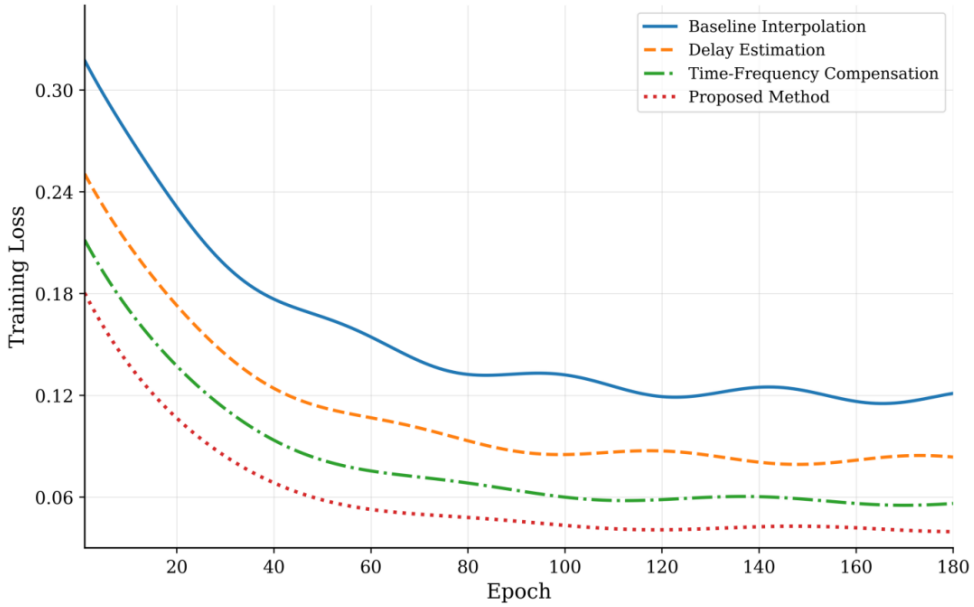

Figure 5: Comparison plot of training loss curves for different algorithms

All the four methods show a relatively fast downward trend in the early stage of training, but there are obvious differences in convergence rate and stability. The basic interpolation method fluctuates greatly in the later stage, and the final loss is maintained at a high level. Although the convergence speed of the delay estimation method is faster than that of the basic interpolation method, there are still local oscillations in the middle and late stages. The decreasing trend of time-frequency compensation method is smoother. The proposed method enters the stable interval at an earlier stage, and the subsequent fluctuation amplitude is minimal. This phenomenon shows that the proposed method can form a more stable parameter update path under the combined effect of synchronous correction, noise suppression and channel consistency constraints, so that the wavelength demodulation and peak discrimination processes have better fitting consistency. The test results show that the wavelength demodulation accuracy of the proposed method reaches 98.9%, and the F1 value of peak identification reaches 97.6%, which are higher than those of other comparison methods. This set of results is consistent with the overall conclusions in the abstract, which also indicates that the algorithm does not sacrifice the integrity of the spectral peak structure while improving the synchronization accuracy.

In order to further reflect the comprehensive differences in the main indicators of different methods, the test results are summarized in Table 3.

Table 3: Comparison of main performance metrics of different algorithms

Method	Synchronization Error / ms	Wavelength Demodulation Accuracy / %	Peak Recognition F1 / %	Variance Suppression Rate / %
Basic Interpolation Method	1.84	93.7	92.1	5.8
Delay Estimation Method	1.12	95.8	94.7	11.6
Time-Frequency Compensation Method	0.63	97.1	96.2	17.9
Proposed Method	0.37	98.9	97.6	21.4

The proposed method achieves the best results in all four indicators. After the synchronization error was reduced to 0.37ms, the comparability of multi-channel signals under the unified time reference was significantly enhanced. The accuracy of wavelength demodulation reaches 98.9%, which indicates that the center wavelength estimation is more stable after correction. The F1 value of peak recognition reached 97.6%, indicating that the boundary of the spectral peak and the position of the main peak could be completely preserved. The variance suppression rate reaches 21.4%, which indicates that the proposed method has stronger convergence ability for cross-channel random fluctuations. Compared with the key data in the abstract, it can be seen that the test results of this section are consistent with the main results of the full paper.

Considering that synchronous signal analysis needs not only to maintain accuracy in ideal scenarios, but also to maintain stable output under noise and local disturbance conditions, this paper continues to perform residual distribution statistics for high noise samples, and the results are shown in Fig. 6.

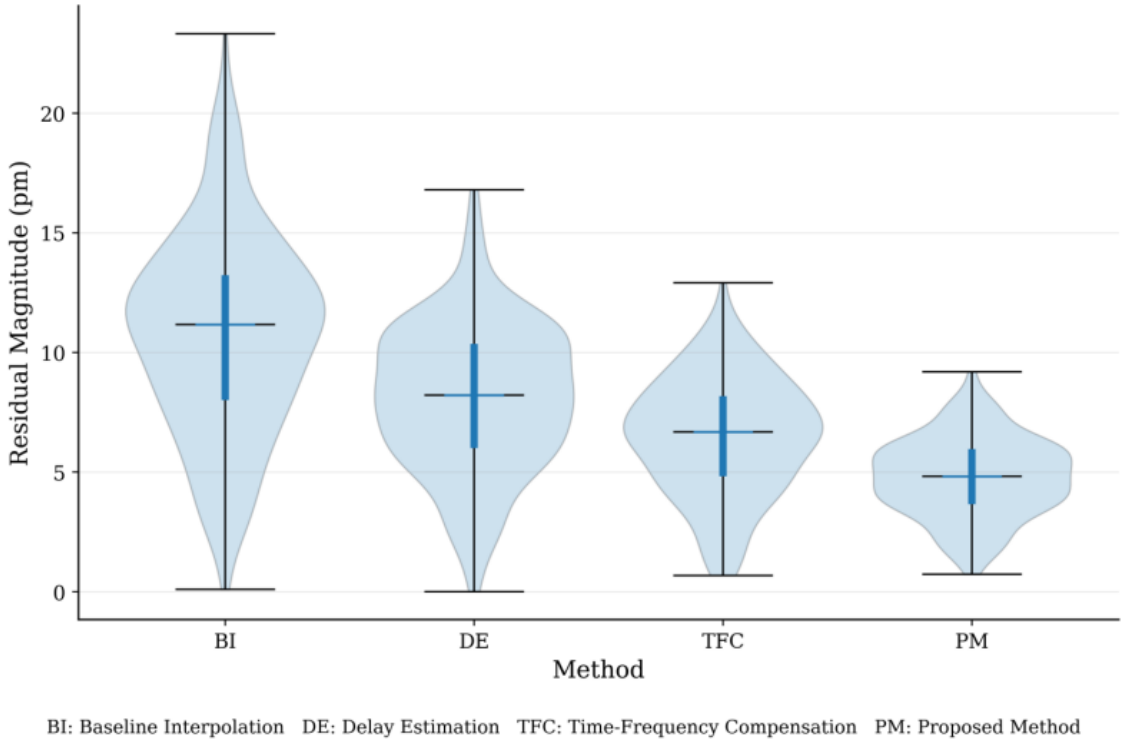

Figure 6: Residual distributions of different algorithms under high noise conditions

Under the condition of high noise, the residual distribution of the basic interpolation method is the most dispersed, and there are many local outliers. Although the delay estimation method compresses part of the offset, there is still an obvious spread in the strong disturbance region. The distribution range of time-frequency compensation method has converged, but the edge residual is still not completely compressed. The residual points of the proposed method are mainly concentrated in the low deviation region, the distribution band is narrower, and the abnormal discrete points are significantly reduced. This result shows that the proposed method can continue to constrain the inter-channel bias through local alignment and consistency update after the completion of time correction, so that the output results maintain strong stability in high noise environments.

In order to further illustrate the retention ability of the algorithm under different noise levels, the wavelength mean square error and consistency score are statistically analyzed, and

the results are shown in Table 4.

Table 4: Test results of the proposed method under different noise conditions

Scenario	Wavelength Mean Squared Error / pm²	Consistency Score	Peak Recognition F1 / %
Low-Noise	5.1	0.963	98.4
Medium-Noise	6.8	0.947	97.9
High-Noise	8.7	0.921	97.1

It can be seen from Table 4 that with the increase of noise intensity, the mean square error of wavelength has increased and the consistency score has slightly decreased, but the overall change range is still in a small range. Even under high noise conditions, the F1 value of peak identification of the proposed method remains at 97.1%, indicating that the algorithm does not lose the main peak information due to local disturbances. Combined with Fig. 6, it can be judged that the advantages of the proposed method in complex scenarios are not only reflected in the single index improvement, but also in the overall convergence of the multi-channel output distribution.

Synthesizing the results in this section, it can be seen that the proposed synchronous signal processing algorithm shows better comprehensive performance in the multi-channel grating sensing system. The proposed method outperforms the comparison methods in terms of average synchronization error, wavelength demodulation accuracy, peak identification integrity, and cross-channel variance control, and the key results are consistent with the summary data. When the synchronization error is reduced to 0.37ms, the multi-channel sequence has a more stable joint analysis foundation. The wavelength demodulation accuracy reaches 98.9%, and the F1 value of peak recognition reaches 97.6%, which indicates that the algorithm can simultaneously take into account time alignment and spectral peak preservation. The variance suppression rate reaches 21.4%, which further indicates that the multi-channel consensus update has practical effect. Based on this algorithm-level test result, the verification of system-level synchronization analysis performance is continued in the next section.

4.2 Performance test of system synchronization analysis

Based on the algorithm level test, this section continues to investigate the system-level synchronization analysis ability, focusing on the observation of multi-channel data organization efficiency, real-time processing ability and result stability. The test platform is deployed in the cooperative environment of 16-channel raster acquisition device and host computer. The sampling frequency is 20 kHz, the window length is 2048 points, the cache adopts the joint structure of dual queue and shared memory, and the number of analysis threads is set to 8. The system ran continuously under five types of load: single channel, 4 channels, 8 channels, 12 channels and 16 channels, and each group lasted for 30 min. The end-to-end delay, effective throughput rate, synchronization completion rate and result consistency score were recorded. All tests were repeated five times and the final results were averaged.

In order to more intuitively reflect the synchronization analysis performance of the system under different concurrent channel conditions, this paper makes statistics on the average delay, effective throughput, synchronization completion rate and consistency score, and the results are shown in Table 5.

Table 5: Experimental results of system synchronization analysis

Number of Concurrent Channels	Average Latency / ms	Effective Throughput ($\times 10^5$ samples/s)	Synchronization Completion Rate / %	Consistency Score
1	8.4	1.2	99.6	0.972
4	9.1	1.8	99.4	0.966
8	10.7	2.3	99.1	0.958
12	11.8	2.6	98.9	0.951
16	12.6	2.8	98.7	0.947

With the increase of the number of concurrent channels, the average delay of the system increases gently, but the increase is always controlled in a small range. The average delay is 8.4 ms under the condition of single channel, and rises to 12.6 ms after expanding to 16 channels, which indicates that the dual-queue scheduling and shared memory transfer can still maintain good data flow organization efficiency in high concurrent scenarios. At the same time, the effective throughput continues to increase with the increase of the number of channels, reaching 2.8×10^5 samples/s under the condition of 16 channels, which indicates that the system can maintain stable output under higher load. The synchronization completion rate remains above 98.7% in each scenario, and the consistency score is always higher than 0.94, indicating that the results do not appear obvious instability in the process of channel expansion.

In order to further observe the distribution characteristics of system delay under different load conditions, this paper counts the average processing delay under the joint effect of cache depth and concurrent channels, and the results are shown in Fig. 7.

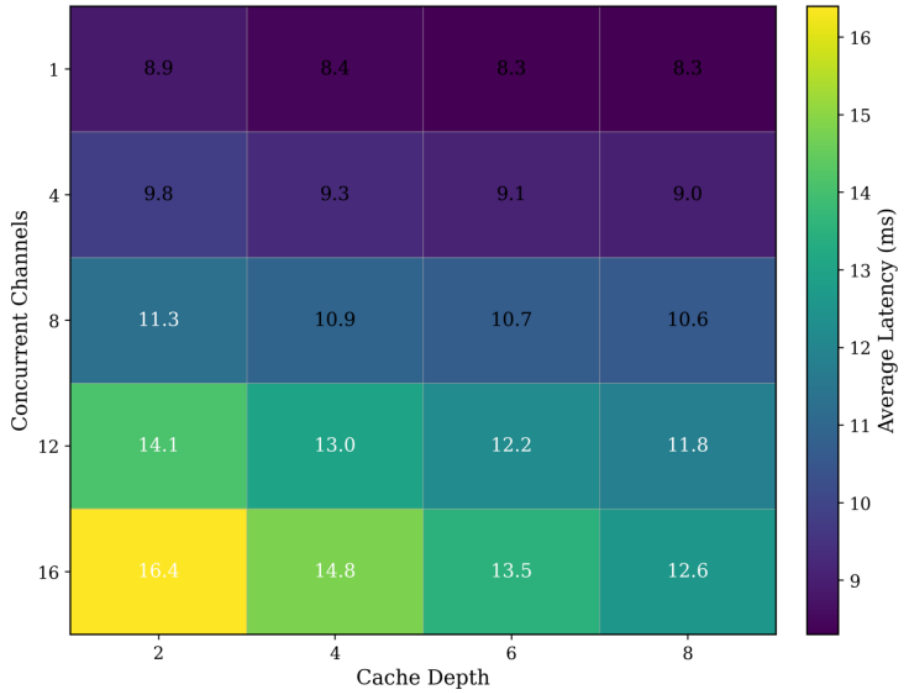

Figure 7: Heat map of system delay distribution under different load conditions

When the concurrent channel is increased from 1 to 8, the system delay changes gently. When the cache depth is increased from 2 to 6, the data block switching and queue refresh are

smoother, and the average delay is stable between 9.8 ms and 11.3 ms. When the number of channels continues to increase to 12 and 16, the write wait will increase significantly if the cache depth is maintained at a low level. When the buffer depth is kept at 8, the system can still control the average latency within 12.6 ms. The results show that the performance of system-level synchronization analysis is not only determined by the sampling frequency, but also closely related to the buffer management strategy and task scheduling mode. The combination of dual-queue and shared memory can effectively absorb the burst pressure caused by high-frequency input, so that the data stream can still be continuous under heavy load conditions.

In order to observe the aggregation characteristics of the system output from the multi-index space, this paper further constructs the 3D scatter distribution plots of end-to-end delay, effective throughput and consensus score, and the results are shown in Fig. 8.

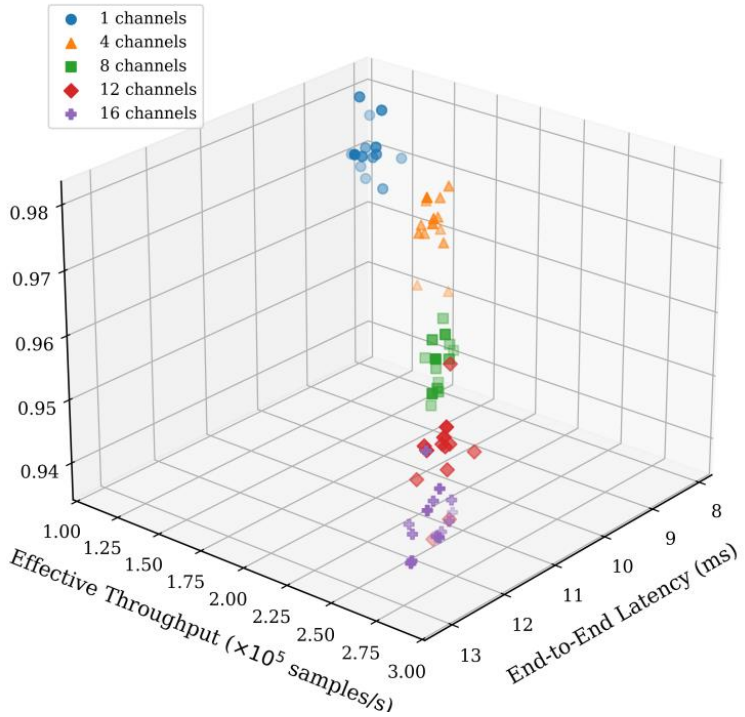

Figure 8: 3D scatter plot of system end-to-end delay, effective throughput, and consistency score

Most of the test samples of the system are distributed in the area of low latency, high throughput and high consistency. The single-channel and 4-channel scenarios are mainly distributed in the area of 8 ms to 10 ms, 1.2×10^5 to 1.8×10^5 samples/s, and consistency score above 0.96. The 8-channel and 12-channel scenarios expand to higher throughput regions, but the point cloud remains concentrated. Although the samples in the 16-channel scenario are slightly extended to the high-load area, the overall distribution is still relatively close, and the consistency score remains above 0.94. The results show that there is no obvious discretization instability after channel expansion, and a good balance between throughput growth and output consistency is formed. The three-dimensional scatter distribution further shows that the system-level synchronization analysis process has strong continuous operation ability under high concurrency conditions.

In order to analyze the source of system performance from the module level, this paper continues to conduct ablation tests on key components, and the test scenario is uniformly set

to 16 channels with high load input. The results are presented in Table 6.

Table 6: Ablation results of key modules of the system

Configuration	Latency / ms	Throughput ($\times 10^5$ samples/s)	Synchronization Completion Rate / %	Consistency Score
Complete System	12.6	2.8	98.7	0.947
Without Dynamic Queue	16.9	2.1	95.8	0.901
Without Consistency Update	12.1	2.8	96.4	0.884
Without Score Compensation	13.8	2.6	97.1	0.912

There are obvious differences in the direction of contribution of different modules to the performance of system-level synchronization analysis. The dynamic queue module has the most direct impact on real-time performance. After removing the dynamic queue module, the system delay increases to 16.9 ms, and the throughput decreases to 2.1×10^5 samples/s, which indicates that cache scheduling plays a major role in traffic shaping under high concurrent inputs. The consensus update module has a relatively limited impact on the delay, but has a significant impact on the synchronization completion rate and consensus score, and the cross-channel output fluctuation increases significantly after removal. After removing the score compensation module, the overall delay increases little, but the synchronization completion rate and consistency score still decrease, which indicates that the fine time shift correction has a continuous support effect on the output quality of the system. It is the synergy between these modules that enables the complete system to maintain a high coherence score in the 16-channel condition.

In order to continue to observe the relationship between the system completion rate and the output scale under different load scenarios, this paper plotted the bubble diagram of the synchronous completion rate and the output data amount, and the results are shown in Fig. 9.

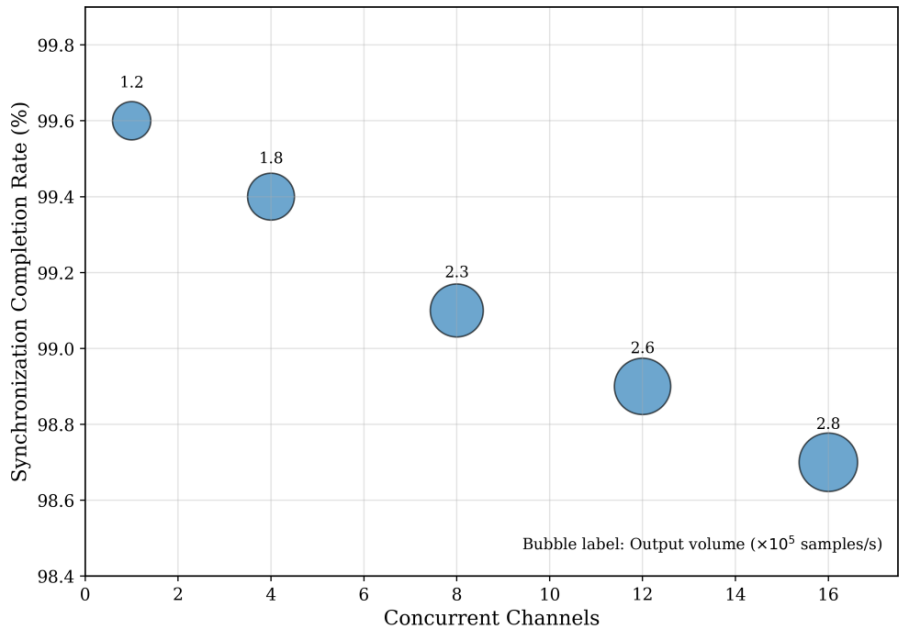

Figure 9: Bubble plots of synchronization completion rate versus output data volume under different load scenarios

The synchronization completion rate of the system is always above 99.1% in the range of 1 to 8 channels, and the bubble size expands with the increase of the number of channels, which indicates that the system throughput expansion has good continuity. After entering the 12-channel and 16-channel scenarios, the synchronization completion rate decreases slightly, but still maintains at 98.9% and 98.7%, respectively. At the same time, the output data per unit time continues to increase, which indicates that the system does not lose effective processing ability due to task backlog under higher load. The distribution results presented by the bubble chart corroborate each other with the statistical data in Table 5 and Table 6, which also shows that the system synchronization analysis process can maintain a relatively stable execution state in the high concurrent input environment.

In summary, the multi-channel grating sensing system maintains a relatively stable operation state in the synchronization analysis task. Even under the high load condition of 16 channels, the average delay of the system is still controlled within 12.6 ms, the effective throughput is 2.8×10^5 samples/s, the synchronization completion rate is 98.7%, and the consensus score is 0.947. The relevant results show that dynamic queue, score compensation and consistency update are not isolated processing units, but work together on data access, time shift correction and result output in the same execution link. After the cooperation of each module, the data transmission between the acquisition layer, the correction layer and the analysis layer is more smooth, and the system can still maintain good real-time response and output stability under the condition of high concurrent input. Based on this test result, the following discussion will further focus on the adaptation performance and operation characteristics under the condition of system expansion.

5 Discussion

The advantages of the proposed method in multi-channel grating synchronization analysis are mainly reflected in the accuracy of time registration, the stability of channel cooperation and the ability of system throughput retention. The results of the algorithm layer show that after the average synchronization error is compressed to 0.37ms, the cross-channel peak position offset is stably limited to a small range, the wavelength demodulation accuracy reaches 98.9%, and the F1 value of peak identification reaches 97.6%, which indicates that a continuous and effective calculation link is formed between delay estimation, score compensation and consensus update. The system layer results further show that under the condition of 16 channels and high load, the average delay is still controlled within 12.6ms, the effective throughput reaches 2.8×10^5 samples/s, the synchronization completion rate remains at 98.7%, and the consensus score is 0.947. This performance does not come from single module hardening, but rather relies on the synergy of cache scheduling, time-shift correction, and result fusion in a unified flow. The corresponding cost is that the scale of the computation graph is enlarged, and the pressure of thread switching and memory access is increased. However, this increase brings more stable synchronization analysis results and stronger multi-channel expansion ability, so it has practical application value. From the perspective of implementation, when the system organizes the acquisition, compensation, analysis and output into a unified data flow, the state transfer between batches is smoother, and the local disturbance will not quickly amplify into global instability. This feature shows that the digital signal processing algorithm for synchronization error suppression not only improves the single demodulation quality, but also enhances the results repeatability and deployment reliability under continuous operation conditions.

6 Conclusions

Focusing on the synchronous signal analysis requirements of multi-channel raster sensing systems, this paper constructs a computational link consisting of synchronous acquisition, digital modeling, error suppression and system-level analysis. Experimental results show that the proposed method can stably complete multi-channel signal alignment under a unified time reference, the average synchronization error is reduced to 0.37ms, the wavelength demodulation accuracy is 98.9%, and the F1 value of peak identification is 97.6%. The average delay of the system can still be controlled within 12.6ms under the condition of 16 channels and high load. The effective throughput of 2.8×10^5 samples/s and the synchronous completion rate of 98.7% are maintained. The above results show that the delay estimation, score compensation, consistency update and buffer scheduling are organized as a unified data flow, and the multi-channel raster signals form a smooth cooperative relationship among the acquisition end, the correction end and the output end. The limitations at this stage are mainly reflected in two aspects. First, the test scene is still dominated by fixed channel scale and laboratory conditions, and the long-term operation data in extreme disturbance environment is still insufficient. Second, although the system has good real-time performance, the overhead of thread switching and memory access will continue to rise at higher concurrency scales. Future research can further introduce adaptive resource scheduling mechanism, lightweight parallel framework and cross-device collaborative analysis strategy, and supplement online learning and edge deployment verification under complex working conditions to enhance the generalization ability, continuous operation ability and large-scale application adaptability of the system in practical engineering. On the whole, this method has engineering application value and continuous optimization space, and can be popularized and applied.

References

[1] Chen S, Yao F, Ren S, et al. Cost-effective improvement of the performance of AWG-based FBG wavelength interrogation via a cascaded neural network[J]. Optics Express, 2022, 30(5): 7647-7663.

[2] Cao Z, Zhang S, Xia T, et al. Spectral demodulation of fiber Bragg grating sensor based on deep convolutional neural networks[J]. Journal of Lightwave Technology, 2022, 40(13): 4429-4435.

[3] Li K, Yuan P, Lu L, et al. PLC-based arrayed waveguide grating design for fiber Bragg grating interrogation system[J]. Nanomaterials, 2022, 12(17): 2938.

[4] Poiana D A, Posada-Roman J E, Garcia-Souto J A. Compact interrogation system of fiber bragg grating sensors based on multiheterodyne dispersion interferometry for dynamic strain measurements[J]. Sensors, 2022, 22(9): 3561.

[5] Huang S, Hu X, Zhang H, et al. A high-precision system of fiber Bragg grating temperature sensing demodulation based on light power detection[J]. Optoelectronics letters, 2022, 18(8): 461-467.

[6] Dey K, Vangety N, Roy S. Machine learning approach for simultaneous measurement of strain and temperature using FBG sensor[J]. Sensors and actuators a: physical, 2022, 333: 113254.

[7] Li S, Ren S, Chen S, et al. Improvement of fiber Bragg grating wavelength demodulation system by cascading generative adversarial network and dense neural network[J]. Applied Sciences, 2022, 12(18): 9031.

[8] Weng S, Yuan P, Lu L, et al. SOI-based arrayed waveguide grating with extended dynamic range for fiber Bragg grating interrogator[J]. Optical fiber technology, 2022, 68: 102815.

[9] Ren S, Chen S, Yang J, et al. High-efficiency FBG array sensor interrogation system via a neural network working with sparse data[J]. Optics Express, 2023, 31(5): 8937-8952.

[10] Li S, Yuan P, Li T, et al. SOI-based 15-channel arrayed waveguide grating design for fiber Bragg grating interrogator[J]. Photonics and nanostructures-fundamentals and applications, 2023, 53: 101113.

[11] Jiao Y, Lin Q, Yao K, et al. Design of high-precision parallel AWG demodulation system[J]. Micromachines, 2023, 14(9): 1662.

[12] Inaba U, Oka H, Kuroda K. Time-and wavelength-division multiplexed interrogation of fiber Bragg gratings based on dual-wavelength differential detection[J]. Optics Communications, 2023, 548: 129871.

[13] Chen Z, Zhuang Y, Meng L, et al. Fully integrated on-chip FBG interrogator for high-accuracy measurement of wavelengths[J]. Optics Letters, 2023, 48(22): 5935-5938.

[14] Yue Z, Li W, Zheng D, et al. Performance enhancement of arrayed waveguide grating-based fibre Bragg grating interrogation assisted by random forest[J]. Electronics Letters, 2023, 59(1): e12682.

[15] Yue Z, Zheng D, Zou X, et al. Large dynamic range interrogation technique for fiber-optic interferometric sensor based on AWG and deep learning algorithm[J]. IEEE Sensors Journal, 2023, 24(1): 278-286.

[16] Hou X, Ren S, Yu K, et al. Federated learning-based wavelength demodulation system for multi-point distributed multi-peak FBG sensors[J]. Optics Express, 2024, 32(23): 41297-41313.

[17] Li S, Yuan P, Li T, et al. High-performance interrogator with bilateral input MMI-based AWG[J]. Optics letters, 2024, 49(3): 454-457.

[18] Ding Z, Chang Q, Deng Z, et al. FBG interrogator using a dispersive waveguide chip and a CMOS camera[J]. Micromachines, 2024, 15(10): 1206.

[19] Liu P, Xu Z, Wang Y, et al. Optimized demodulation of highly overlapped fiber Bragg grating sensor networks using two-stage deep learning approach[J]. Optical Engineering, 2024, 63(4): 046103-046103.

[20] Xu R, Yuan P, Yang Y, et al. A multi-channel AWG-based FBG interrogation system using a 1× 4 MEMS optical switch[J]. Optical Fiber Technology, 2024, 88: 104004.